



## Original Research Paper

## Numerical study on particle deposition in rough channels with different structure parameters of rough elements

Wenpeng Hong, Xin Wang\*, Jianxiang Zheng

School of Energy and Power Engineering, Northeast Electric Power University, Jilin 132012, China



## ARTICLE INFO

## Article history:

Received 10 August 2017

Received in revised form 26 May 2018

Accepted 10 August 2018

Available online 24 August 2018

## Keywords:

Gas-solid two phase flow  
Particle deposition  
Rib-roughened channel

CFD

## ABSTRACT

This paper presents a study of the characteristics of particle deposition in rib-roughened channels. The gas-particle flow was numerically investigated by Reynolds stress model (RSM) with the discrete particle model (DPM). The particle deposition velocity and deposition ratio at different positions were numerically investigated in a channel where the relative roughness factor,  $e/D$ , were between 0.02 and 0.1, and the ratios of rough-element spacing to its height,  $p/e$ , were between 7 and 20. It is found that the eddy structures behind the rough-elements are changed by the increase of  $e/D$ . The windward surfaces are the main deposition regions and the cavities between the rough-elements are the secondary deposition regions.  $e/D$  contributes more to the increase of particle deposition velocity than  $p/e$ .

© 2018 The Society of Powder Technology Japan. Published by Elsevier B.V. and The Society of Powder Technology Japan. All rights reserved.

## 1. Introduction

With the rapid development of industry, increasing energy consumption and the rising number of vehicles, particle pollution (also known as particulate matter) in the atmospheric environment has become the leading cause of pollution in big cities [1]. According to investigation statistics, urban residents spend more than 20 h indoors. However, health problems resulting from indoor air quality (IAQ) have also become increasingly prominent; thus, the prevention and control of indoor air pollution have become an important health issue, especially for those with asthma and other respiratory problems. Atmospheric particulates not only enter houses through air conditioning and ventilation, but also deposits in the interior of the pipe, and provide nutrition for the breeding of bacteria and fungus. Microorganisms produce secondary suspension with the action of air flow, which spreads to the indoor environment, causing its air quality to deteriorate even further [2,3]. Roughness elements widely exist in ventilation ducts, air conditioner components, heat exchangers, and electrostatic precipitators. These elements not only improve the flow and heat transfer effect, but also intercept particulate matter effectively [4].

Particle transport and deposition has received extensive attention recently. Deshmukh et al. [5] used the high speed particle tracking velocimetry to measure particle velocity distribution, they found smaller particles to be the best choice for channel distribu-

tion and that better homogeneity in the flow could be achieved through a lower mass loading ratio and higher gas velocity. Laein et al. [6] used the PIV to investigate the TiO<sub>2</sub>-water nanofluid free convection. They found that the nanoparticles will decrease the velocity boundary layer. Kussin and Sommerfeld [7,8] experimentally studied the wall roughness effects on particle behavior in duct flow by phase-Doppler anemometry (PDA). The deposition of micron-droplets in rectangular tubes was studied by Barth et al. [9], who also studied multilayer particle deposition in a channel arranged periodic steps by experiment [10]. Particle deposition in turbulent flow has been widely simulated by computational fluid dynamics (CFD) [11–13]. Moreover, it can provide more detailed information about the flow field and particle behavior than experimental measurements [14,15]. Abdolzadeh et al. [16,17] numerically analysed the deposition velocity of particles on tilted rough surfaces by a modified v2-f turbulence model with a two-phase Eulerian approach. They found that a thermophoretic force and tilt angle can have a significant effect on particle deposition velocity. De Marchis et al. [18] investigated the effect of roughness on particle distribution based on direct numerical simulation (DNS) and the Euler-Lagrange method. Li et al. [19] used the coupled discrete element method (DEM) and CFD approach to investigate the solid deposition in pipes. Lericain et al. [20,21] researched multilayer particle deposition in an obstructed channel by numerical simulation. They used a detached eddy simulation (DES) with self-organized criticality to reproduce the growth of a multilayer deposit. Because the direct numerical simulation (DNS) or large eddy simulation (LES) is too computationally expensive, it still

\* Corresponding author.

E-mail address: [2201500318@neepu.edu.cn](mailto:2201500318@neepu.edu.cn) (X. Wang).

## Nomenclature

$C_c$	Cunningham slip correction factor	$Re_y$	Reynolds number of y-coordinate
$C_D$	drag coefficient	$S$	ratio of particle-to-fluid density
$D$	channel diameter (m)	$U_0$	average velocity of air (m/s)
$D_h$	hydraulic diameter of channel (m)	$u$	velocity of fluid (m/s)
$d_p$	particle diameter (m)	$u_p$	velocity of particle (m/s)
$e$	rough-element height (m)	$u_f$	frictional velocity of air (m/s)
$f_{rl}$	friction factor of the smooth channel	$V_d^+$	non-dimensional deposition velocity
$f_r$	friction factor of rib-roughened channel	$V_d$	particle deposition velocity (m/s)
$L$	the length of channel (m)		
$N_{dep}$	particle deposition numbers to wall		
$N_{in}$	incoming particle numbers		
$N_d$	the number of deposited particles on surface		
$N_t$	the number of particles that transited through the section upon the deposit surface		
$p$	rough-element spacing (m)		
$R_d$	particle deposition ratio		
$Re$	Reynolds number		
$Re_p$	particle Reynolds number		

<i>Greek symbols</i>	
$\varepsilon$	turbulence dissipation rate (J/(kg·s))
$\mu$	dynamic viscosity of air (Pa·s)
$\rho$	air density (kg/m <sup>3</sup> )
$\rho_p$	particle density (kg/m <sup>3</sup> )
$v$	kinetic viscosity of air (m <sup>2</sup> /s)
$\tau_w$	shear stress on the wall (Pa)
$\tau_p^+$	non-dimensional particle relaxation time

cannot be widely used for engineering applications. The Reynolds-averaged Navier-Stokes (RANS) model became the preferred choice. Different methods of simulating particle deposition in channel flow are compared by Tian and Ahmadi [22]. They found that compared with other RANS models, the Reynolds stress model (RSM) can calculate the particle deposition rate more accurately as it considers the anisotropy of turbulence. Recently, Lu and Lu [23] numerically studied the particle deposition characteristics in duct which arranged ribs on the underside. Moreover, the influence of rib shapes, rib spacing and height, and surface rib arrangements were also considered in their later researches [24–26]. However, previous research was mainly about overall particle deposition rate. Few study researched the particle deposition ratio on each rough element in the initial stage of gas-solid flow. The local particle deposition ratio and the effect of rib spacing and height have not been well investigated. Therefore, further study is recommended.

In this paper, particle deposition on surfaces with different spacing and height rough-elements was investigated by the RSM turbulence model with the Lagrangian tracking method. The purpose of this study is to investigate the effect of rough-element spacing and height on particle deposition and get the detail information of particle deposition ratio on each rough element in the initial stage of two phase flow. Moreover, the mechanisms of particle deposition by a rib-roughened surface and the characteristics of local deposition were also analysed. All findings are presented herein.

## 2. Physical model and computational cases

A schematic of this study's exemplary two-dimensional computational rough channel is shown in Fig. 1. The rough channel is 20 mm high and 400 mm long. To insure the full development of turbulent flow before the rough section, the first half of the channel is smooth. The second half of the channel underside has rough-elements uniformly arranged with identical spacing. The rough-element is characterized by  $p/e$  and  $e/D$ , which are the ratios of rough-element spacing to its height and rough-element height to channel diameter, respectively. Here,  $p$  is the rough-element spacing,  $e$  is the rough-element height and  $D$  is the channel diameter.

A variety of rough channel were simulated in this paper, and the parameters and layout of the rough-elements are shown in Table 1.

## 3. Numerical method and validation

### 3.1. Numerical model

#### 3.1.1. Continuous phase

Since the velocity of the turbulent air flow is low, it can be considered an incompressible fluid. For turbulent air flow, the mean mass and momentum equations can be expressed as,

$$\frac{\partial \bar{u}_i}{\partial x_i} = 0 \quad (1)$$

$$\frac{\partial \bar{u}_i}{\partial t} + \bar{u}_j \frac{\partial \bar{u}_i}{\partial x_j} = -\frac{1}{\rho} \frac{\partial \bar{p}}{\partial x_i} + \frac{1}{\rho} \frac{\partial}{\partial x_j} (\mu \frac{\partial \bar{u}_i}{\partial x_j} - \rho \bar{u}'_i \bar{u}'_j) \quad (2)$$

where  $\bar{u}_i$  is the time-average velocity,  $x_i$  is the space position,  $t$  is the time,  $\bar{p}$  is the time-averaged pressure,  $\rho$  is the constant air density, and  $\mu$  is the dynamic viscosity.

In this study, the individual turbulent was solved using the RSM model. The differential transport equation is given as,

$$\begin{aligned} \frac{\partial}{\partial t} (\bar{u}'_i \bar{u}'_j) + \bar{u}_k \frac{\partial}{\partial x_k} (\bar{u}'_i \bar{u}'_j) &= \underbrace{\frac{\partial}{\partial x_k} \left( \frac{\nu_t}{\sigma_k} \frac{\partial \bar{u}'_i \bar{u}'_j}{\partial x_k} \right)}_{\text{convective transport}} - \underbrace{\left( \bar{u}'_i \bar{u}'_k \frac{\partial \bar{u}_j}{\partial x_k} + \bar{u}'_j \bar{u}'_k \frac{\partial \bar{u}_i}{\partial x_k} \right)}_{D_{T,jj} = \text{diffusive transport}} \\ &\quad - \underbrace{P_{ij} = \text{stress production}}_{P_{ij} = \text{stress production}} \\ &\quad \times \underbrace{-C_1 \frac{\varepsilon}{k} \left[ \bar{u}'_i \bar{u}'_j - \frac{2}{3} \delta_{ij} k \right]}_{\phi_{ij} = \text{pressure strain}} - C_2 \left[ P_{ij} - \frac{2}{3} \delta_{ij} P \right] - \underbrace{\frac{2}{3} \delta_{ij} \varepsilon}_{\varepsilon_{ij} = \text{dissipation}} \end{aligned} \quad (3)$$

where the  $\sigma_k = 1.0$ ,  $C_1 = 1.8$ , and  $C_2 = 0.6$  are the empirical constants [27]. The turbulence dissipation rate,  $\varepsilon$ , is as follow,

$$\frac{\partial \varepsilon}{\partial t} + \bar{u}_j \frac{\partial \varepsilon}{\partial x_j} = \frac{\partial}{\partial x_j} \left[ \left( v + \frac{\nu_t}{\sigma_\varepsilon} \right) \frac{\partial \varepsilon}{\partial x_j} \right] - C_{\varepsilon 1} \frac{\varepsilon}{k} \bar{u}'_i \bar{u}'_j \frac{\partial \bar{u}_i}{\partial x_j} - C_{\varepsilon 2} \frac{\varepsilon^2}{k} \quad (4)$$

where the empirical constants  $\sigma_\varepsilon = 1.3$ ,  $C_{\varepsilon 1} = 1.44$ ,  $C_{\varepsilon 2} = 1.92$  [28].

#### 3.1.2. Discrete phase

In this paper, particle phase is considered a discrete phase and its motion is simulated by the discrete particle model. Because the ratio of particle volume to air volume in the whole channel is 0.08% in this paper, far less than 5%, the influence of particles on turbulent air flow is ignored and so is the interactions between particles [29,30]. Moreover, the particle-to-gas density ratio is so

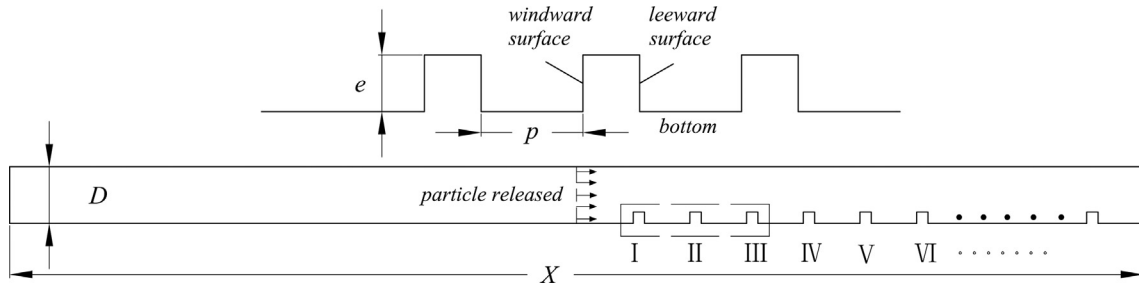


Fig. 1. Schematic of rough channel with rough-elements.

**Table 1**  
Computational cases.

Case no.	D (mm)	p/e	e/D	e (mm)	p (mm)	Rough-element number	d <sub>p</sub> (μm)
1	20	Smooth					3, 5, 10, 20, 30, 40
2	20	10	0.02	0.4	4	49	10
3	20	10	0.04	0.8	8	24	10
4	20	10	0.07	1.4	14	13	10
5	20	10	0.1	2	20	9	3, 5, 10, 20, 30, 40
6	20	7	0.04	0.8	5.6	35	10
7	20	14	0.04	0.8	11.2	17	10
8	20	17	0.04	0.8	13.6	14	10
9	20	20	0.04	0.8	16	12	10

large that the pressure gradient force and the virtual mass force are not considered in this paper. The particle-phase governing equation is as follow.

$$m_p \frac{du_{pi}}{dt} = \frac{\pi d_p^2}{8} C_D \rho |u_i - u_{pi}| (u_i - u_{pi}) + m_p \frac{g_i (\rho_p - \rho)}{\rho_p} + 1.61 (\mu \rho)^{1/2} d_p^2 (u_i - u_{pi}) \left| \frac{\partial u_i}{\partial x_i} \right|^{1/2} \quad (5)$$

Here,  $u_i$  is the fluid velocity including fluctuation, and  $u_{pi}$  is the particle velocity.  $\rho$  and  $\rho_p$  are the density of fluid and particle, respectively. The drag force, the gravity and buoyancy force and the Saffman's lift force are considered on the right side of Eq. (5). All particles are assumed to be solid spheres and the particle rotation is not considered. The Magnus force and the Brownian force are ignored.

$C_D$  is the drag coefficient [31], and it is defined as follows.

$$C_D = 24/Re_p, \quad \text{for } Re_p < 1 \\ C_D = 24(1 + 0.15Re_p^{0.687})/Re_p, \quad \text{for } 1 < Re_p < 400 \quad (6)$$

Here  $Re_p$  is the particle Reynolds number, it can be calculated from

$$Re_p = \frac{\rho d_p |u - u_p|}{\mu} \quad (7)$$

### 3.1.3. Boundary conditions and solution methods

The velocity inlet and outflow were chosen to be set as the boundary conditions. The boundary condition of the wall is no-slip. And the wall boundary condition was set up by enhanced wall treatment. It combines the two-layer zonal model with the enhanced wall function. The two-layer model [32] is used to describe the near wall characteristics of the fluid. It uses the  $Re_y$  to divide the near wall zone into two layers. The calculation method of  $Re_y$  is as follows:

$$Re_y = \frac{y\sqrt{k}}{v} \quad (8)$$

For the region of  $Re_y > 200$ , the simulation of the flow field can be calculated by the traditional  $k-\epsilon$  model or the RSM model. For

the region of  $Re_y < 200$ , the Wolfshtein's one-equation model [33] is used to simulate. In this region, the momentum equation and the turbulent kinetic energy equation are consistent with the traditional  $k-\epsilon$  model or the RSM model, while the turbulent diffusion rate  $\epsilon$  and eddy viscosity  $v_{t,2layer}$  are calculated by the following formula:

$$\epsilon = \frac{k^{3/2}}{l_\epsilon} \quad (9)$$

$$v_{t,2layer} = C_\mu \sqrt{k} l_\mu \quad (10)$$

The enhanced wall treatment is a combination of the  $v_{t,2layer}$  in the two-layer zonal model with the  $v_t$  of the high Reynolds number defined in the external region. The equation is as follows:

$$v_{t,enh} = \lambda_e v_t + (1 - \lambda_e) v_{t,2layer} \quad (11)$$

More details of the enhanced wall treatment can be found in Ansys Fluent 15. The air dynamic viscosity  $\mu$  is  $1.789 \times 10^{-5}$  kg·s/m. The air density is  $1.225 \text{ kg/m}^3$ . The inlet air velocity is set at 5 m/s.

For the discrete particulate phase, the particle density is  $2450 \text{ kg/m}^3$ . Twenty-thousand particles were released at the halfway point in the channel, i.e.,  $X = 200 \text{ mm}$ , where the air flow is fully developed. The initial velocity of the particles is assumed to be equal to the average air velocity. The particles were assumed to be deposited when they touched the lower wall and reflected when they touched the upper wall. The restitution coefficient for particle collision with upper wall and lower wall are assumed to be 1.0 and 0, respectively. The particles that not deposit on the lower wall escape through the outlet of channel.

The finite volume method was adopted to discretize the governing equations. The convection terms and the diffusion terms are discretized by the second-order scheme and the central differencing scheme, respectively. The coupling of velocity and pressure used the SIMPLE Algorithm. All simulations are performed by the commercial software Ansys-Fluent.

### 3.2. Mesh and model validation

#### 3.2.1. Grid resolution

The whole computational domain was partitioned by structured grids. The mesh refinement technique was used near the rough-elements and wall to obtain an accurate turbulent flow field in the boundary layer. There is a 0.05 mm distance between the first grid and the walls. The grid growing factor is set as 1.2 from the surface to the center in a longitudinal direction. The boundary layer mesh consists of five layers. Furthermore, the validation of grids-independent was made. The different test mesh numbers for Case 5 are 85,144, 101,020, 136,400, 153,927, 215,000. The average air velocity at the windward section of VIII rough element was used as the monitoring parameter. The results are shown in Fig. 2, it can be found that the calculation results with mesh number more than 136,400 are almost consistent. Therefore, the suitable mesh number is 136,400. The same method was used to make the validation of grids-independent for all cases. From Case 1 to Case 9, the mesh numbers are 39,200, 376,950, 251,064, 195,120, 136,400, 392,975, 296,755, 277,915, 252,405 in the order given. Fig. 3 shows a closer view of the structural grids between rough element.

#### 3.2.2. Model validation

In order to verify the correctness of the model in this study, the air flow in smooth channel and rib-roughened channel with the

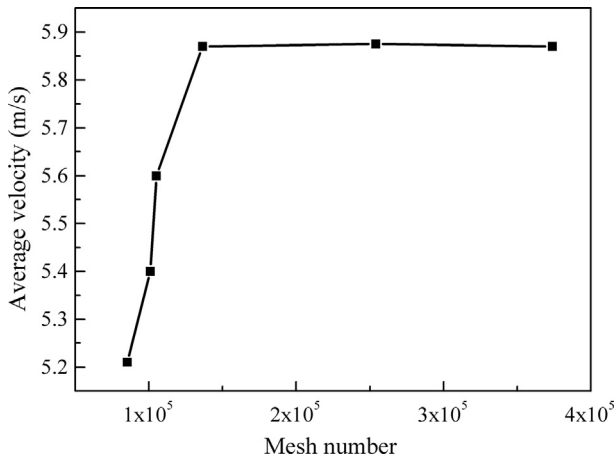


Fig. 2. Grid independence verification.

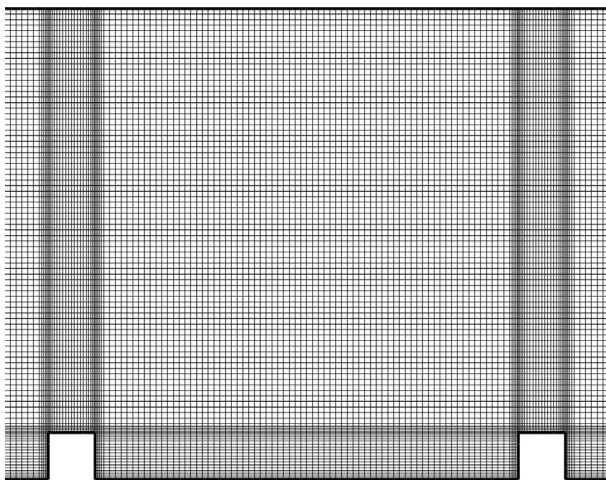


Fig. 3. Structural grids between rough element.

parameter,  $p/e = 10$ ,  $e/D = 0.1$ , were investigated, respectively. The ratio of friction factor  $fr/fr_l$  were adopt to make the validation. Here  $fr_l$  is the friction factor of the smooth channel,  $fr$  is the friction of rib-roughened channel and  $Re$  is Reynolds number. The friction factors of the smooth channel and rib-roughened channel are defined as,

$$fr_l = 0.316 Re^{-0.25} \quad (12)$$

$$fr = \frac{\Delta P D_h}{1/2 \rho U_0^2 L} \quad (13)$$

where  $\Delta P$  is the pressure drop between inlet and outlet,  $D_h$  is the hydraulic diameter,  $U_0$  is the average velocity of the channel flow and  $L$  is the length of channel.

And the Reynolds number  $Re$  can be written as

$$Re = \frac{U_0 D \rho}{\mu} \quad (14)$$

The results are compared with the experiment results by Karwa [34], as shown in Fig. 4 where the ratio of friction factor between our results and the Karwa results is very consistent. This proves that the present turbulent air flow field in a rib-roughened channel can be simulated accurately by the RSM model.

To further verify the validity of the model used in this paper, the flow field around the rough element of Case 5 was investigated. Fig. 5 shows that streamlines near the VIII rough element, it can be seen that there were four eddies near the rough element. The  $L_{1,2,3,4}$  represent the length of each eddy, respectively. The ratio of eddy length to element height were compared with DES data of Lecrivain et al. [20], the experiment date of Casarsa and Arts [35] and the LES data of Lohász et al. [36], as shown in Table 2. It can be found that the result match well with the previous studies. The correctness of the model used in this paper is further verified.

#### 3.3. Computation of particle deposition velocity and ratio

Usually the curves of non-dimensional deposition velocity versus non-dimensional particle relaxation time are used to present the results of deposition calculations [37]. This method is adopted in this paper, and the deposition velocity is defined as [38],

$$V_d = -\frac{DU_0 \ln(1 - N_{dep}/N_{in})}{L} \quad (15)$$

where  $N_{dep}$  is the number of particles which are deposited on the surface and  $N_{in}$  is the number of incoming particles.

The non-dimensional deposition velocity is defined as,

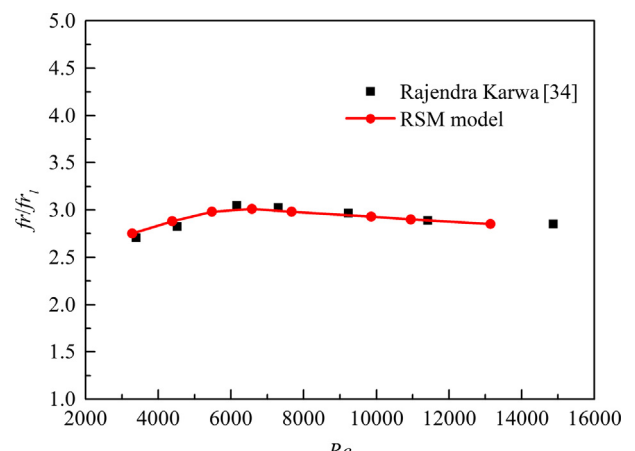
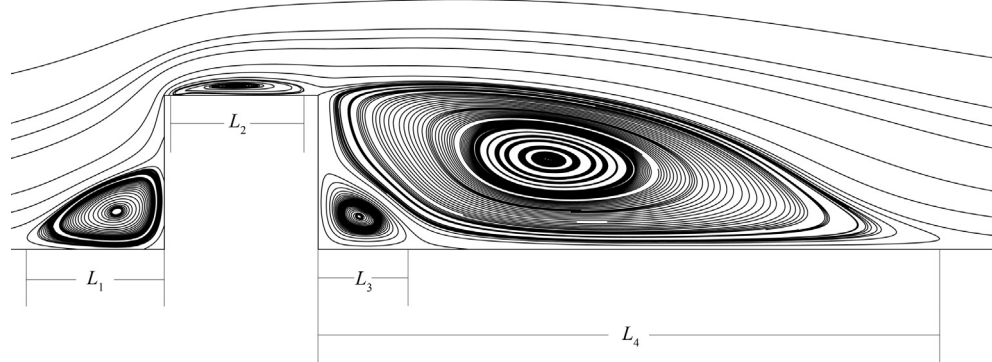


Fig. 4. Validation of friction factor ratio ( $fr/fr_l$ ) evolution according to  $Re$ .



**Fig. 5.** Streamlines near the rough element of Case 5.

**Table 2**  
Comparison of eddy lengths with previous studies.

	$L_1/e$	$L_2/e$	$L_3/e$	$L_4/e$
RSM (present study)	0.9	0.85	0.6	4.1
DES [20]	1.06	0.81	0.88	4.12
Experiment [35]	1–1.5	0.6–0.9	0.2–0.3	3.7–3.9
LES [36]	1.62	0.91	0.5	3.45

$$V_d^+ = V_d/u^* \quad (16)$$

where  $u^*$  is the frictional velocity. It can be calculated by,

$$u^* = \sqrt{\tau_w/\rho} \quad (17)$$

and the non-dimensional particle relaxation time is written as,

$$\tau_p^+ = \frac{Sd_p^2 u^{*2}}{18\nu^2} C_c \quad (18)$$

$S$  is the particle-to-gas density ratio.  $C_c$  is the Cunningham slip correction factor [39], and can be given as,

$$C_c = 1 + \frac{2\lambda}{d} [1.257 + 0.4e^{-(1.1d_p/2\lambda)}] \quad (19)$$

To observe the particle deposition for different cases more clearly, a deposition ratio  $R_d$  was defined as Eq. (20),

$$R_d = \frac{N_d}{N_t} \times 100\% \quad (20)$$

where  $N_d$  is the number of deposited particles on surface,  $N_t$  is the number of particles that transited through the section upon the deposit surface.

## 4. Results and discussion

### 4.1. Flow field

The turbulent air flow field in the rib-roughened channel is compared with the smooth channel in Fig. 6. From Fig. 6(b), it can be seen that the rough elements suddenly narrow the flow duct, and enhance the air velocity in the center area of duct to nearly 140% of the inlet velocity. Furthermore, the rough elements disturb the original boundary layer. The centerline flow velocity at  $X = 200$  mm was adopt as the inflow velocity of rough section. The new boundary layer thickness is shown in Fig. 7. It can be found that the bottom boundary layer thickness increases with the increase of rough elements; the top boundary layer thickness first decreases and then increases with the increase of rough elements. Moreover, the rough elements make the bottom boundary layer much thicker than the top boundary layer.

As shown in Table 1, there are 49, 24, 13, 9, 34, 16, 13 and 11 rough elements on the underside of the channel for Case 2 to Case 9, respectively. As the flow field is stable after the IV rough element, the flow field between VII and VIII rough elements is chosen for investigation, as shown in Fig. 8. From Fig. 8(a), two eddies appear between the rough elements when  $e/D = 0.02$ . The rough elements narrowed the flow channel and enhanced the flow velocity. Moreover, there is a low-velocity with high-pressure area before the windward surfaces of the rough elements, and a low-velocity with a low-pressure area behind the leeward surfaces of the rough elements. Therefore, a large-scale separation eddy and a relatively small attachment eddy simultaneously appear in each repeated cavity, as shown in Fig. 8(a). But, when the  $p/e$  is constant, the increase of  $e/D$  makes the height and the spacing of rough elements become larger at the same time. A secondary eddy is

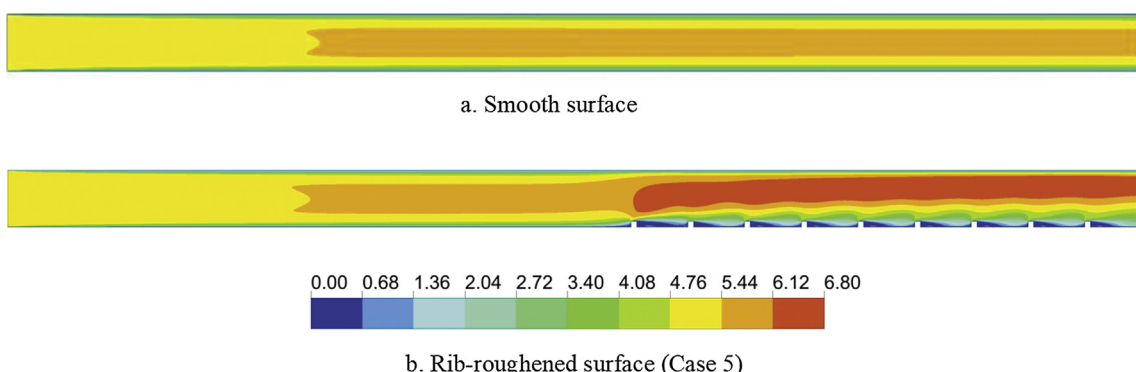


**Fig. 6.** Velocity fields of smooth and rib-roughened surface ( $U_0 = 5$  m/s).

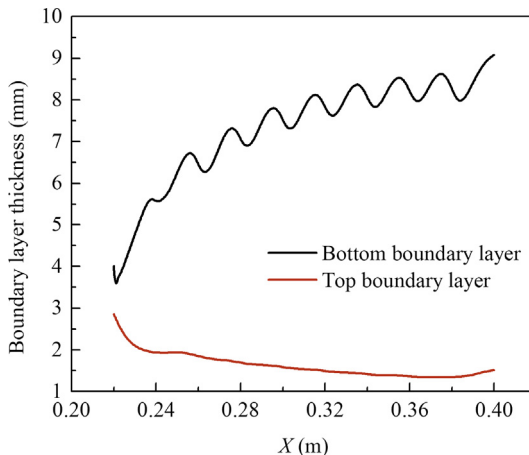


**Fig. 7.** Boundary layer thickness of Case 5 ( $U_0 = 5 \text{ m/s}$ ).

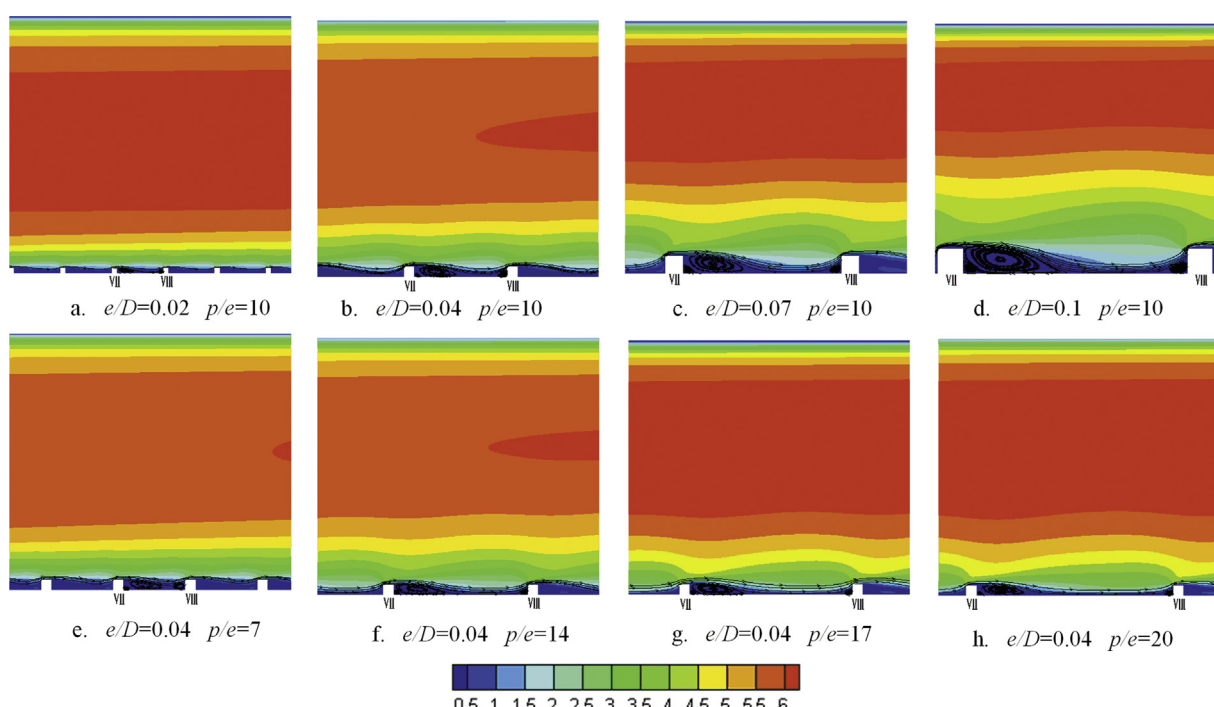
perceived in the leeward corner as the reverse flow approaches the vertical surface as shown in Fig. 8(b)–(h). The total number of eddies in the repeated cavity increased to 3. Moreover, when  $p/e$  is fixed, the maximum flow velocity increases with the increase of  $e/D$ , as shown in Fig. 9. The increase of  $e/D$  makes the flow duct become narrower and then causes the enhancement of maximum flow velocity. When  $e/D$  is fixed, the maximum flow velocity decreases with the increase of  $p/e$ , as shown in Fig. 10. The larger  $p/e$  indicates a larger effective height of the flow duct and the maximum flow velocity will decrease.

#### 4.2. Effects of rough-elements spacing and height on particle deposition ratio

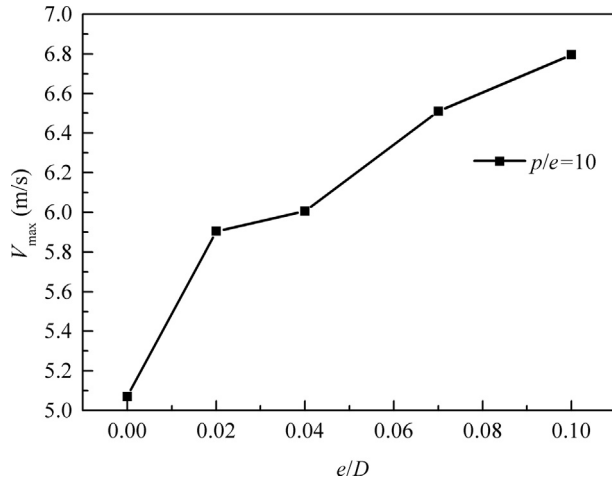
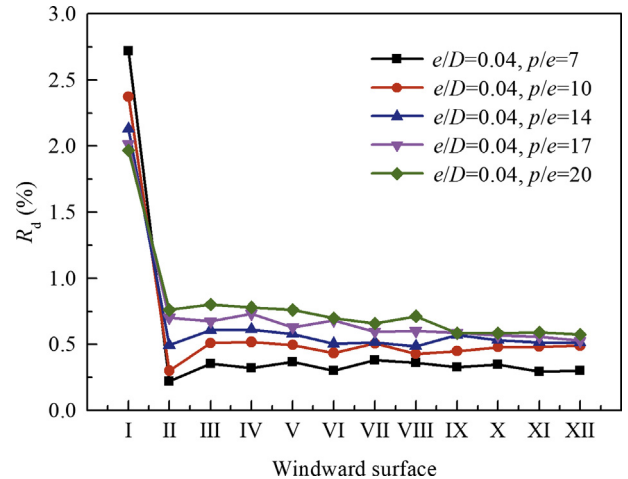
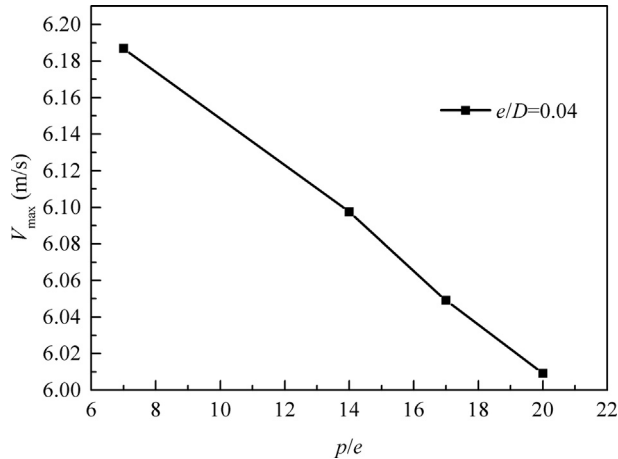
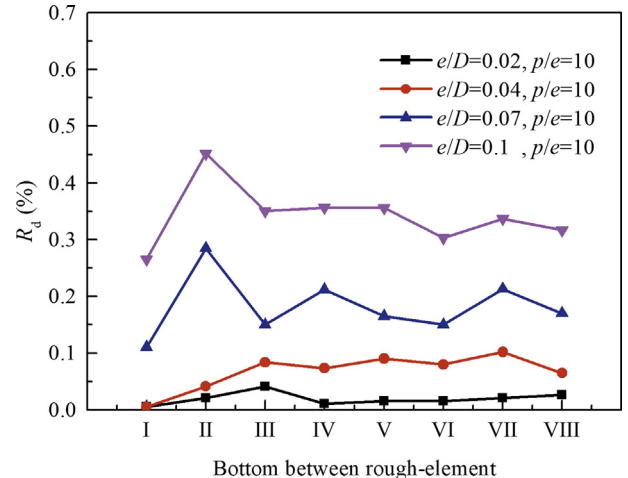
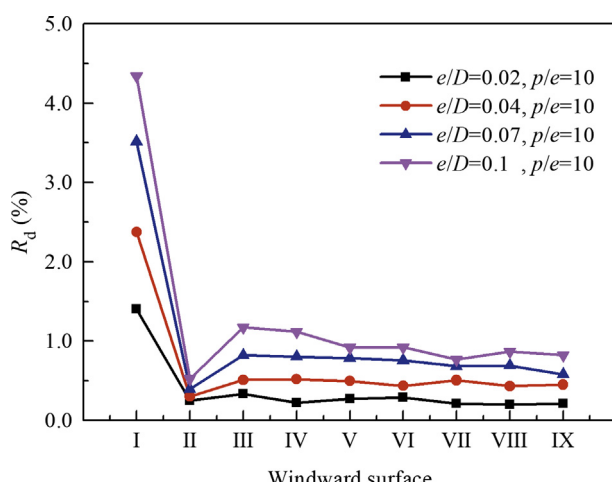
As shown in Table 1, there are only nine rough elements in Case 5 and the gas-solid two phase flows have reached their fully developed state after IV rough element, the particle deposition at the first nine windward surfaces were chosen to be analysed. Fig. 11

shows the deposition ratio on windward surfaces with different  $e/D$  when  $p/e = 10$ . Fig. 12 shows the deposition ratio on windward surfaces with different  $p/e$  when  $e/D = 0.4$ . For every case, the deposition ratio on I windward surface is maximum, then it drops rapidly on the II windward surface. The deposition ratio tends to stabilize from the III windward surface. As the particles were released at  $X = 200 \text{ mm}$ , the particles failed to respond the interception of the windward surface at I rough element. It makes a large number of particles deposit on I windward surface. Meanwhile, as the influence of rough elements to flow field structure, the turbulent vortex gradually changed from small to large. Therefore, the deposition ratio on II windward surface drops rapidly, and the deposition ratio on III-IX windward surfaces remains almost unchanged. Fig. 11 shows that the deposition ratio increases with the enhancement of  $e/D$  when  $p/e = 10$ . The height of rough elements can be represented by  $e/D$ , and the increase of  $e/D$  indicates an increase in rough elements' height. The intercept area is larger when the  $e/D$  is bigger; meanwhile, the interception effect for particles is strengthened, and the deposition ratio is increased. From Fig. 12, it can be observed that the deposition ratio on windward surface increases with the increase of  $p/e$ . The increase of  $p/e$  makes the rough element spacing become larger, and weakens the drag force. It weakens the air carrying effect on particles, and enhances the ability of particles to escape from the airflow and deposit on surfaces. Hence the deposition ratio is increased.

Fig. 13 shows the deposition ratio on bottom between two adjacent rough elements with different  $e/D$  when  $p/e = 10$ . When  $e/D = 0.02$ , the spacing of rough elements is minimum, so is the bottom deposition area between two adjacent rough elements. Meanwhile, there are almost no particles deposited on the bottom between the two adjacent rough elements. The deposition ratio on the bottom increases with the increase of  $e/D$ . Comparing the results in Fig. 11 with those in Fig. 13, it can be seen that the deposition ratio on windward surface is four times that on bottom between the two adjacent rough elements for the same Case. Fig. 14 shows the deposition ratio on bottom between two adjacent rough elements with different  $p/e$  when  $e/D = 0.04$ . The deposition



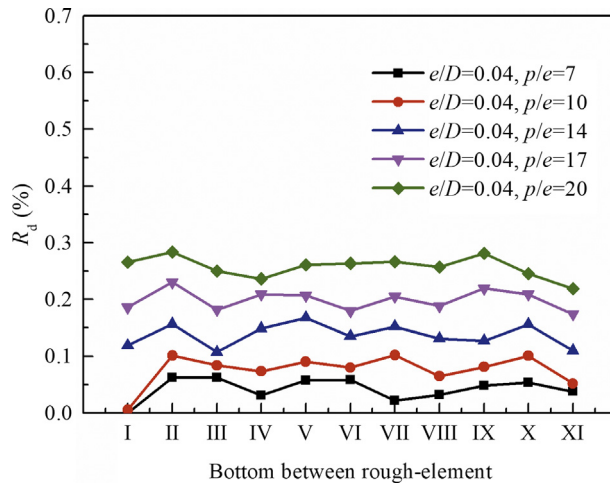
**Fig. 8.** Velocity fields for different  $e/D$  and  $p/e$ .

Fig. 9. Maximum flow velocity in channel for different  $e/D$ .Fig. 12. Deposition ratio on windward surfaces with different  $p/e$ .Fig. 10. Maximum flow velocity in channel for different  $p/e$ .Fig. 13. Deposition ratio on bottom between rough-elements with different  $e/D$ .Fig. 11. Deposition ratio on windward surfaces with different  $e/D$ .

ratio on the bottom increases with the increase of  $p/e$  when the relative roughness remained unchanged. Meanwhile, the deposition ratio is almost linear with  $p/e$ . Comparing the results in Figs. 12 and 14, it can be observed that, when the flow field is stable, the smaller the  $p/e$  is, the smaller the difference between rate deposition ratio on windward and bottom becomes.

#### 4.3. Effects of rough-elements spacing and height on particle deposition velocity

Fig. 15 shows the non-dimensional particle deposition velocities for Case 1, and the results were in very good agreement with the experimental results by El-Shobokshy [40]. Therefore, the model used in this paper can predict the particle deposition velocity accurately. Eq. (18) shows that the increase of particle diameter will lead to a rapid increase in relaxation time. As shown in Fig. 15, the increase of non-dimensional particle relaxation makes the non-dimensional deposition velocity gradually increase, but the increase rate gradually decreases and finally the rate is almost equal to 0. The main reason for this trend is that, according to the summary of Wood [41], the interaction between particles and the turbulent eddy is the main reason for particle deposition when the particle diameter is small ( $10^{-1} < \tau_p^+ < 10$ ). When  $\tau_p^+ > 10$ , the effect of the turbulent eddy capture and entrainment for particles are weakened by the increase of the particle diameter; furthermore, the particle inertia plays a major role in the deposition of large particles. Fig. 16 shows the validation of non-dimensional particle deposition velocity on rough surface. It can be seen the curves of the results have the same trend, but the  $V_d^+$  of Lecrivain et al. [21] is larger than the present result. The reason may be that their model is three-dimensional, including particle deposition on the side and upper wall.



**Fig. 14.** Deposition ratio on bottom between rough-elements with different  $p/e$ .

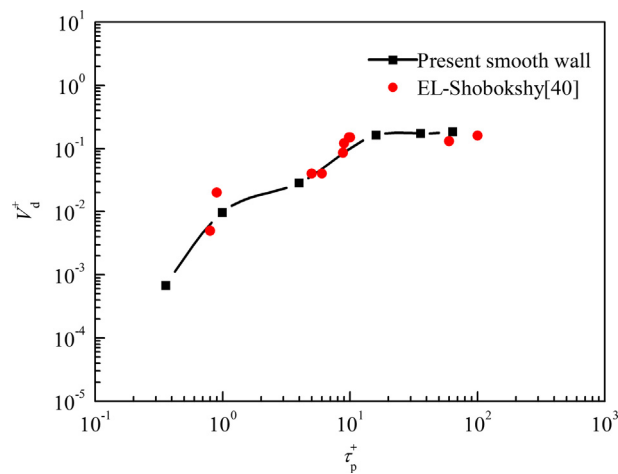


**Fig. 15.** Validation of non-dimensional particle deposition velocity on smooth surface.

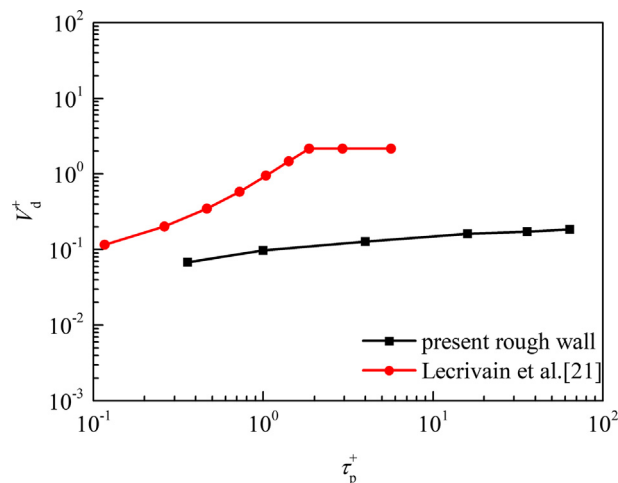


**Fig. 16.** Validation of non-dimensional particle deposition velocity on rough surface.

The non-dimensional particle deposition velocity with different  $p/e$  and  $e/D$  are shown in Fig. 17 and Fig. 18, respectively. It can be seen that, when the  $e/D$  keeps constant the particle deposition

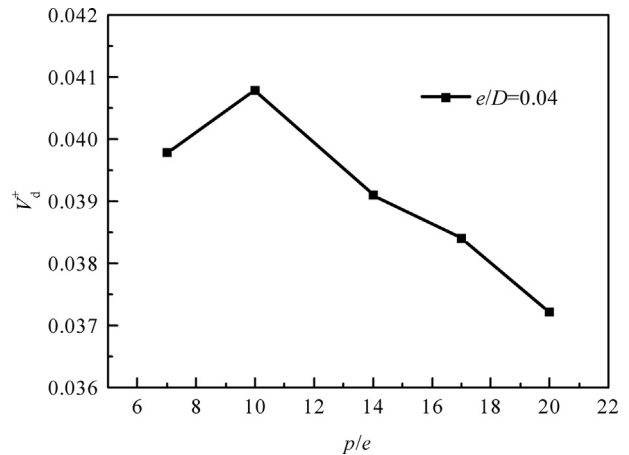


**Fig. 17.** Non-dimensional particle deposition velocity with different  $p/e$ .

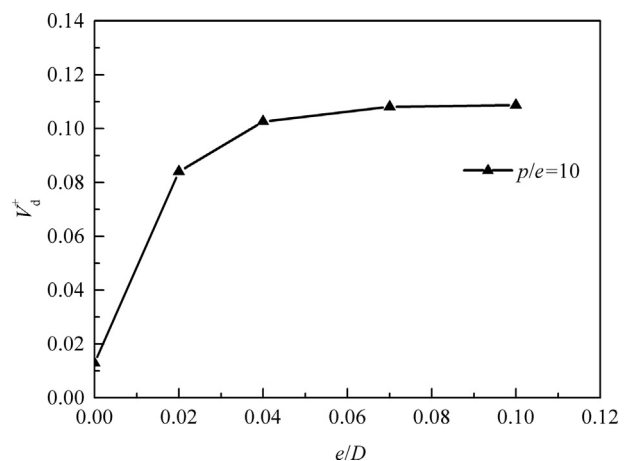


**Fig. 18.** Non-dimensional particle deposition velocity with different  $e/D$ .

velocity reaches a maximum when  $p/e = 10$  and it decreases with the increase of  $p/e$ . Although the trend is to decline, the decline is not great. The particle deposition velocity at  $p/e = 10$  is only 0.004 greater than when  $p/e = 20$ . When the  $p/e$  keeps constant, the particle deposition velocity presents the same trend as  $e/D$ . When the  $e/D$  reaches 0.1, the particle deposition velocity remains almost constant. After a general comparison, it can be seen that the  $e/D$  has a greater influence on particle deposition velocity than  $p/e$ .

## 5. Conclusions

The research presented herein represents an investigation of the deposition characteristics of particles in a channel with different rough-element spacings and heights. These were investigated numerically by RSM and DPM models. The mechanisms of particle deposition were analysed. Furthermore, the deposition ratios at different positions were discussed for different cases. The conclusions are as follow,

1. The existence of the rough element increases the thickness of the boundary layer near the roughness element. With the increase of  $e/D$ , the number of eddies in the cavity between two adjacent element changes from 2 to 3 and the effect of the turbulent eddy entrainment on particles are enhanced.
2. The windward surface of rough elements is the main deposition area, and the bottom between two adjacent elements is the secondary deposition area. The deposition ratio on the channel

- bottom increases with the increase of  $p/e$  and  $e/D$ . The deposition ratio on the windward surface increases with the increase of  $e/D$  and  $p/e$ .
3. The relative roughness  $e/D$  has a greater influence on the particle deposition velocity than  $p/e$ . The particle deposition velocity increases with the increase of  $e/D$ . When  $e/D$  reaches 0.1, the particle deposition velocity varies very slightly with  $e/D$ . Meanwhile, the particle deposition velocity reaches a maximum at  $p/e = 10$  when  $e/D$  is kept constant.

## Acknowledgement

This study was funded by the National Natural Science Foundation of China (No. 51776032).

## References

- [1] Q. Yao, S.Q. Li, H.W. Xu, J.K. Zhuo, Q. Song, Studies on formation and control of combustion particulate matter in China: a review, *Energy* 34 (2009) 1296–1309.
- [2] A.D. Kappos, P. Bruckmann, T. Eickmann, N. Englert, U. Heinrich, P. Höpke, E. Koch, G.H. Krause, W.G. Kreyling, K. Rauchfuss, Health effects of particles in ambient air, *Int. J. Hyg. Environ. Health* 207 (2004) 399–407.
- [3] A. Seaton, D. Godden, W. MacNee, K. Donaldson, Particulate air pollution and acute health effects, *Lancet* 345 (1995) 176–178.
- [4] J.S. Yong, S.K. Sang, Effect of obstructions on the particle collection efficiency in a two-stage electrostatic precipitator, *J. Aerosol Sci.* 27 (1996) 61–74.
- [5] A. Deshmukh, V. Vasava, A. Patankar, M. Bose, Particle velocity distribution in a flow of gas-solid mixture through a horizontal channel, *Powder Technol.* 298 (2016) 119–129.
- [6] R.P. Laein, S. Rashidi, J.A. Esfahani, Experimental investigation of nanofluid free convection over the vertical and horizontal flat plates with uniform heat flux by PIV, *Adv. Powder Technol.* 27 (2016) 312–322.
- [7] J. Kussin, M. Sommerfeld, Experimental studies on particle behaviour and turbulence modification in horizontal channel flow with different wall roughness, *Exp. Fluids* 33 (2002) 143–159.
- [8] M. Sommerfeld, J. Kussin, Wall roughness effects on pneumatic conveying of spherical particles in a narrow horizontal channel, *Powder Technol.* 142 (2004) 180–192.
- [9] T. Barth, G. Lericain, U. Hampel, Particle deposition study in a horizontal turbulent duct flow using optical microscopy and particle size spectrometry, *J. Aerosol Sci.* 60 (2013) 47–54.
- [10] T. Barth, M. Reiche, M. Banowski, M. Oppermann, U. Hampel, Experimental investigation of multilayer particle deposition and resuspension between periodic steps in turbulent flows, *J. Aerosol Sci.* 64 (2013) 111–124.
- [11] Q. Chen, Ventilation performance prediction for buildings: a method overview and recent applications, *Build. Environ.* 44 (2009) 848–858.
- [12] H. Jiang, L. Lu, K. Sun, Simulation of particle deposition in ventilation duct with a particle-wall impact model, *Build. Environ.* 45 (2010) 1184–1191.
- [13] K. Sun, L. Lu, H. Jiang, A computational investigation of particle distribution and deposition in a 90° bend incorporating a particle-wall model, *Build. Environ.* 46 (2011) 1251–1262.
- [14] N.P. Gao, J.L. Niu, Modeling particle dispersion and deposition in indoor environments, *Atmos. Environ.* 41 (2007) 3862–3876.
- [15] K. Sun, L. Lu, H. Jiang, A numerical study of bend-induced particle deposition in and behind duct bends, *Build. Environ.* 52 (2012) 77–87.
- [16] M. Abdolzadeh, M.A. Mehrabian, Combined effect of thermophoretic force and other influencing parameters on the particle deposition rate on a tilted rough surface, *Int. J. Therm. Sci.* 50 (2011) 954–964.
- [17] M. Abdolzadeh, M.A. Mehrabian, A. Soltani, Goharrizi, Numerical study to predict the particle deposition under the influence of operating forces on a tilted surface in the turbulent flow, *Adv. Powder Technol.* 22 (2011) 405–415.
- [18] M. De Marchis, B. Milici, G. Sardina, E. Napoli, Interaction between turbulent structures and particles in roughened channel, *Int. J. Multiphase Flow* 78 (2016) 117–131.
- [19] J. Li, C. Webb, S.S. Pandiella, G.M. Campbell, T. Dyakowski, A. Cowell, D. McGlinchey, Solids deposition in low-velocity slug flow pneumatic conveying, *Chem. Eng. Process.* 44 (2005) 167–173.
- [20] G. Lericain, L. Barry, U. Hampel, Three-dimensional simulation of multilayer particle deposition in an obstructed channel flow, *Powder Technol.* 258 (2014) 134–143.
- [21] G. Lericain, D.-M. Sevan, B. Thomas, U. Hampel, Numerical simulation of multilayer deposition in an obstructed channel flow, *Adv. Powder Technol.* 25 (2014) 310–320.
- [22] L. Tian, G. Ahmadi, Particle deposition in turbulent duct flows—comparisons of different model predictions, *J. Aerosol Sci.* 38 (2007) 377–397.
- [23] H. Lu, L. Lu, Numerical investigation on particle deposition enhancement in duct air flow by ribbed wall, *Build. Environ.* 85 (2015) 61–72.
- [24] H. Lu, L. Lu, Effects of rib spacing and height on particle deposition in ribbed duct air flows, *Build. Environ.* 92 (2015) 317–327.
- [25] H. Lu, L. Lu, A numerical study of particle deposition in ribbed duct flow with different rib shapes, *Build. Environ.* 94 (2015) 43–53.
- [26] H. Lu, L. Lu, CFD investigation on particle deposition in aligned and staggered ribbed duct air flows, *Appl. Therm. Eng.* 93 (2016) 697–706.
- [27] B.E. Launder, G.J. Reece, W. Rodi, Progress in the development of a Reynolds-stress turbulence closure, *J. Fluid Mech.* 68 (1975) 537–566.
- [28] B.E. Launder, D.B. Spalding, Lectures in Mathematical Models of Turbulence, Academic Press, London, 1972.
- [29] J.K. Eaton, J.R. Fessler, Preferential concentration of particles by turbulence, *Int. J. Multiphase Flow* 20 (1994) 169–209.
- [30] B. Wang, H.Q. Zhang, X.L. Wang, Large eddy simulation of particle response to turbulence along its trajectory in a backward-facing step turbulent flow, *Int. J. Heat Mass Transf.* 49 (2006) 415–420.
- [31] W.C. Hinds, *Aerosol Technology: Properties, Behavior, and Measurement of Airborne Particles*, Wiley, New York, 1984.
- [32] H.C. Chen, V.C. Patel, Near-wall turbulence models for complex flows including separation, *AIAA J.* 26 (1988) 641–648.
- [33] M. Wolfshtein, The velocity and temperature distribution in one-dimensional flow with turbulence augmentation and pressure gradient, *Int. J. Heat Mass Transf.* 12 (1969) 301–318.
- [34] R. Karwa, Experimental studies of augmented heat transfer and friction in asymmetrically heated rectangular ducts with ribs on the heated wall in transverse, inclined, V-continuous and V-discrete pattern, *Int. Commun. Heat Mass Transf.* 30 (2003) 241–250.
- [35] L. Casarsa, T. Arts, Experimental investigation of the aerothermal performance of a high blockage rib-roughened cooling channel, *J. Turbomach.* 127 (2005) 580–588.
- [36] M.M. Lohász, P. Rambaud, C. Benocci, Flow features in a fully developed ribbed duct flow as a result of MILES, *Flow Turbul. Combust.* 77 (2006) 59–76.
- [37] A. Guha, A unified Eulerian theory of turbulent deposition to smooth and rough surfaces, *J. Aerosol Sci.* 28 (1997) 1517–1537.
- [38] H. Liu, L. Zhang, Prediction of particle deposition characteristic in 90° square bend: square bend particle deposition characteristic, *Appl. Therm. Eng.* 31 (2011) 3402–3409.
- [39] H. Ounis, G. Ahmadi, Analysis of dispersion of small spherical particles in a random velocity field, *J. Fluids Eng.* 112 (1990) 114–120.
- [40] M.S. El-Shobokshy, Experimental measurements of aerosol deposition to smooth and rough surfaces, *Atmos. Environ.* 17 (1983) 639–644.
- [41] N.B. Wood, A simple method for the calculation of turbulent deposition to smooth and rough surfaces, *J. Aerosol Sci.* 12 (1981) 275–290.